Advanced Steel Construction – Vol. 21 No. 3 (2025) 243–252
DOI:10.18057/IJASC.2025.21.3.6

SEISMIC BEHAVIOR AND RESIDUAL SEISMIC CAPACITY OF CORRODED DOUBLE-STEEL-PLATE COMPOSITE SHEAR WALL

Jian Li [1,*], Bo-Kai Chen [1], Zhe Zhao [1], Gang Gao [2] and Yan Wang [1]

[1] *School of Civil Engineering, Qingdao University of Technology, Qingdao, 266033, China*
[2] *Yantai Jinjian Engineering Design Co, Ltd, Yantai, Shandong 264000, China*
** (Corresponding author: E-mail: 1_li@qut.edu.cn)*

ABSTRACT

In long-term aggressive corrosion environments, steel structures are susceptible to corrosion, which can significantly impair their mechanical performance. The seismic behavior of the corroded double-steel-plate composite shear wall (DSCW) is investigated in this paper. The parameters investigated include the corrosion rate, steel plate thickness, axial compression ratio, and concrete strength. The corroded DSCW model was established using ABAQUS's secondary development function. The research results show that: local corrosion under cyclic loading may cause the steel plate to buckle prematurely, resulting in early concrete crushing and failure of the binding bars; The hysteresis curve of the corroded specimen shows a distinct "pinching" effect; With the increase of corrosion rate, the bearing capacity and ductility of DSCW decrease obviously. The optimal steel plate thickness for seismic performance is identified as 9 mm, while higher concrete strength correlates with enhanced bearing capacity; Increasing the axial compression ratio leads to a gradual decrease in bearing capacity. A shear capacity formula that accounts for corrosion rates is proposed, and the relationship between the residual seismic capacity and drift, in terms of energy dissipation, is also analyzed. Finally, the study calculates the reinforceable residual drift limits for DSCW damaged by earthquakes.

ARTICLE HISTORY

Received: 27 August 2024
Revised: 6 January 2025
Accepted: 8 January 2025

KEYWORDS

Double-steel-plate composite shear wall;
Seismic performance;
Local corrosion;
Finite element simulation;
Residual seismic capacity

1. Introduction

The double-steel-plate composite shear wall (DSCW) comprises of exterior steel plates, in-filled concrete, and mechanical connectors. Recently, DSCW has become widespread use as lateral force-resisting elements in high-rise buildings and nuclear power plants [1-2]. However, when exposed to corrosive environments, the exterior steel plates become susceptible to corrosion, which causes damage to the surface and makes the DSCW less able to handle earthquakes. Therefore, we need to explore how DSCW behaves during earthquakes after it has corroded.

The performance of the DSCW is largely determined by the bond between the steel plates and the concrete. Insufficient confinement between these materials may cause premature buckling of the steel plates [3]. Various connectors have been proposed to enhance the bond, including connectors with different shapes [4-10]. Zhang and Chen [11,12] proposed DSCW with shear bolts, stiffeners, and L-shaped connectors. It should be noted that these connectors require extensive welding, which may induce deformation and residual stresses. The DSCW connector selected in this study uses a binding bar, which is a bolt-based connection method. The constraint rod can be installed quickly and conveniently, without the need for welding. Zhu et al. [10] proposed the DSCW with binding bars and found that reducing the spacing between the binding bars effectively enhances the seismic performance of the DSCW. Although the seismic performance of DSCW has attracted significant attention, research on their seismic performance after corrosion remains limited.

Corrosion seriously affects the strength of steel, leading to significant degradation. A lot of research has been done to understand how corrosion affects steel. Imperatore et al. [13] studied how even corrosion affects the constitutive relationships of steel rebars. Sun et al. [14] found that in addition to uniform corrosion, random pitting corrosion also occurred in steel rebars. Pitting damage caused stress concentrations in steel bars, leading to varying degrees of degradation in their mechanical properties. Qin and Jin [15,16] conducted both experimental investigations and numerical simulations to assess the impact of corrosion on steel. Their results indicated that the decrease in the mechanical properties of the steel was linked to the loss of cross-sectional area in the steel, leading to substantial changes in the yield plateau, which ultimately resulted in decreased strength and ductility. Ren et al. [17] highlighted that the presence of pitting, particularly under conditions of nonuniform corrosion, caused localized stress concentrations, which expedited the failure of the steel. These studies, employing both experimental and numerical approaches, offer valuable insights into the degradation patterns of corroded steel. Although most of these studies have focused on the corrosion of individual steel members, they provide a solid foundation for understanding the mechanical behavior of composite structures exposed to corrosion.

Recent years have seen a surge in research examining the performance of corroded composite structures, particularly targeting Concrete-Filled Steel Tubes (CFST). Yang et al. [18] investigated the mechanical properties of CFST subjected to both uniform and local corrosion. Local corrosion is a common occurrence in practical engineering, prompting numerous studies on the mechanical behavior of CFST under such conditions [19-23]. Scholars have simulated local corrosion by introducing surface defects in steel tubes to assess their impact. Huang et al. [24] found that artificial notches, whether vertical or slanted, significantly reduced the peak resistance and ductility of the steel tubes. However, horizontal notches had a lesser impact on peak resistance and ductility, primarily causing global flexural buckling. Zhong et al. [25] observed that local defects in the steel tubes causing a shift in the specimen's centroid and a subsequent decrease in the bearing capacity of CFST. While simulating local defects effectively replicated the mechanical properties after local corrosion, it differed significantly from the damage observed in CFST under real corrosion environments. To bridge this gap, Xue et al. [26] designed CFST specimens subjected to NaCl solution and atmospheric corrosion. An accurate finite element (FE) model was developed based on 3D scanning profile data, revealing that corrosion exhibited fractal characteristics and significantly reduced the specimen's ductility. Corrosion-induced circumferential expansion often led to steel pipe fractures, further diminishing ductility. Zhang et al. [27] found that corrosion of the outer steel pipe significantly reduced the axial bearing capacity and plastic deformation capacity of CFST. As the corrosion ratio increased, the mechanical properties further decreased. Significant progress has been made in the aforementioned literature, which is critical for improving the design of CFST. However, few studies have been conducted on corroded DSCW in steel-concrete structures. Therefore, investigating the seismic performance of corroded DSCW is essential for evaluating its service life. Current codes also lack design methods for corroded DSCW. Therefore, studying the seismic performance of corroded DSCW is of significant meaning for assessment the service life of corroded DSCW.

DSCW are critical components in resisting lateral forces and are subjected to cyclic loading, necessitating a thorough investigation into their seismic performance after corrosion. This paper mainly studies the seismic performance of corroded DSCW with binding bars. Corrosion patterns were categorized into uniform corrosion and random pitting, based on relevant standards and corrosion tests on steel plates. Consequently, the model considers local uniform corrosion and random pitting on the exterior steel plates. A detailed parameter analysis is subsequently conducted to examine the mechanical characteristics of the corroded DSCW. Based on finite element calculations, a formula for calculating corroded DSCW bearing capacity is proposed. Considering the risk of seismic events affecting already damaged members, the study proposes a seismic damage evaluation method for DSCW, based on residual drift and residual seismic capacity post-earthquake. Furthermore, the study proposes limit values for evaluation indices to ensure the reinforced capacity of these structural members post-earthquake.

2. FE model establishment and verification

2.1. Design of local corrosion specimen model

Research on DSCW has primarily focused on their seismic performance with various connectors. However, a gap remains in understanding the mechanical behavior and failure modes of these shear walls under cyclic loading in corrosive environments. This study investigates the seismic performance of DSCWs with binding bars under cyclic loading after corrosion. Nonlinear static analysis methods were employed to comprehensively explore and elucidate the seismic behavior of these shear walls under varying corrosion levels. Under typical atmospheric conditions, steel plates corrode initially, forming areas with specific maximum residual thicknesses that later develop local pitting corrosion. According to the studies by Wang et al. [28] and using formulas derived from the mean values of corrosion pits, equations were fitted to estimate the uniform corrosion thickness and the diameter of pitting pits as the corrosion rate varies, shown in Fig. 1 and Eq. (1). Using these formulas, the uniform corrosion thickness and mean values of pitting pits for steel plates with corrosion rates of 10%, 15%, and 25% were determined. To realistically simulate the seismic performance of DSCWs under local corrosion, random functions in Python software were used to generate random corrosion pits on steel plates, as shown in Fig. 2. This approach ensures that the corrosion simulation captures the varied and unpredictable nature of pitting corrosion's effects on structural performance.

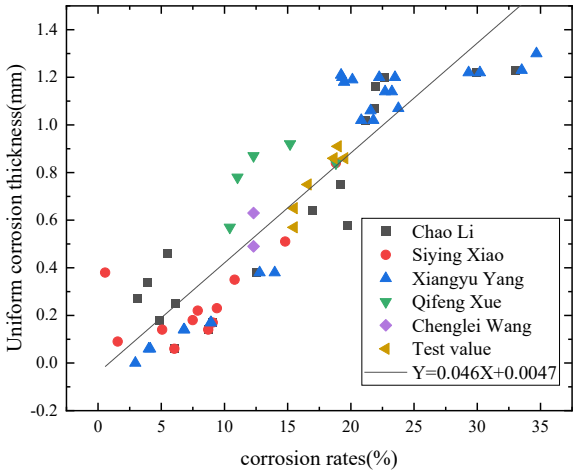

Fig. 1 The uniform corrosion thickness changes with the corrosion rates to fit the formula

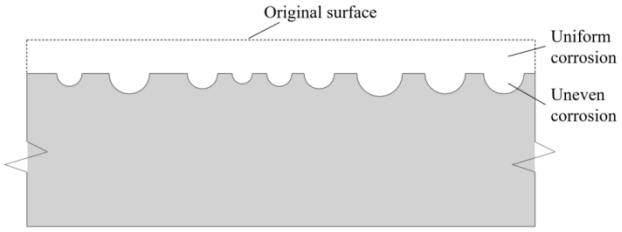

Fig. 2 The Python software's random function generates random rust pits on the steel plate

$$\mu_D = 0.729 + 0.041\rho_V \quad R^2=0.713 \tag{1a}$$

$$\sigma_D = 0.526 + 0.034\rho_V \quad R^2=0,789 \tag{1b}$$

where μ_D is the average diameter of the corrosion pits, σ_D is the standard deviation of the diameter of the pit, ρ_V is the local volume loss rate.

We focus on the numerical simulation of pitting randomness during the construction of the geometric model. Geometric modeling serves as the core of the simulation methodology. Previous studies have shown that the shape of corrosion pit has little effect on the mechanical properties of the structure. [29,30], so we chose a circular pit to simulate pitting. The locations of these pits were determined using Python's Random function, which defined the distribution of pitting. A Boolean operation was subsequently applied to generate the final geometric model, based on the relationship between the generated array of storage forms and the corresponding position vector array. The flowchart is shown in Fig. 3.

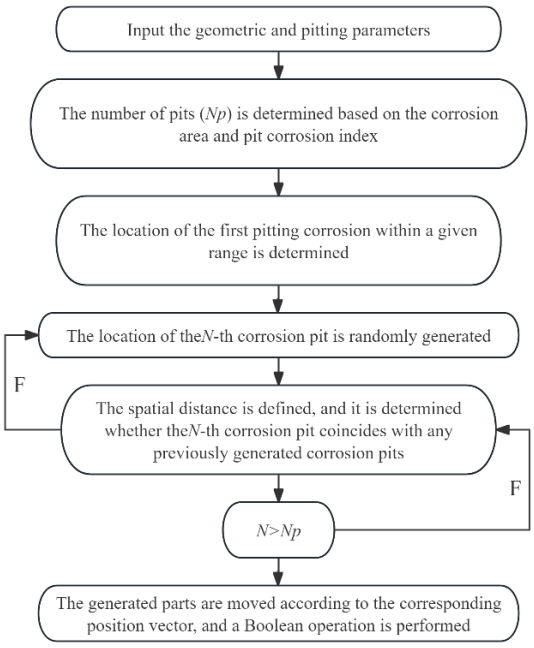

Fig. 3 The flow chart of modeling process

2.2. Material properties

2.2.1. Steel

In this study, steel was modeled using the isotropic elastic-plastic model in ABAQUS software. This model effectively describes the metal's plastic characteristics and satisfies the Von-Mises stress yield criterion. The stress-strain relationship follows the five-fold line model detailed in "Steel Pipe Concrete Structures" [31] by Zhong.

2.2.2. Concrete

In order to simulate the mechanical behavior of concrete, the concrete damage plasticity model in ABAQUA is adopted. This model was chosen based on yield surfaces proposed by Lubliner [32] and Lee [33], with an additional cracking energy criterion defined by Hillerborg et al. [34]. Han's [35] stress-strain relationship for concrete tension was adopted. The tensile cracking and compressive failure of concrete can be well simulated by using the corresponding stress-strain relationship in ABAQUS.

2.2.3. Element type and interaction

During the meshing process, the end plates, binding bars, and concrete were meshed using hexahedral elements. Due to pitting corrosion on the steel plate's surface, hexahedral meshing was applied to the non-corroded areas, while tetrahedral meshing was used for the corroded regions of the steel plates. The meshing of each part is shown in Fig. 4.

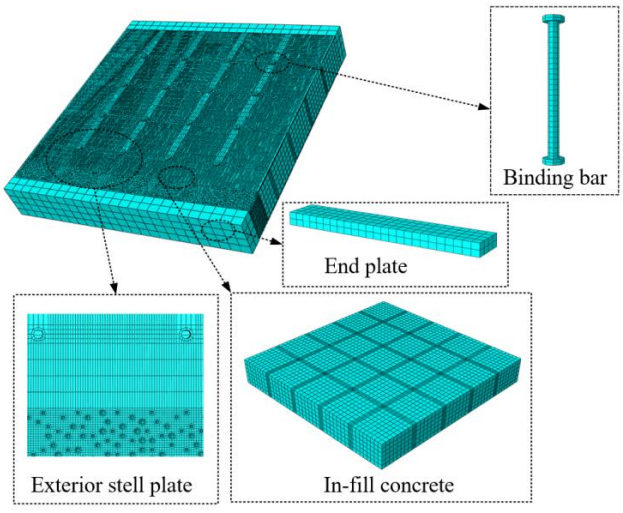

Fig. 4 FE model

The following interaction relationships were defined: “Tie” constraints were applied between the end plates and the concrete, still between the end plates and the steel plate. Frictional constraints were applied between the steel plate and concrete, with the coefficient of friction set to 0.6. The same contact setting was applied between the binding bars and the concrete. Frictional contact was defined between steel plates and binding bars, with the coefficient of friction is set to 0.3.

2.3. Boundary conditions

The loading process takes place in two stages. In the first stage, axial pressure is applied, followed by the application of horizontal load in the second stage. The lower end plate of the shear wall is fully fixed to prevent any movement. The upper end plate is coupled to the reference point. To prevent out-of-plane instability of the DSCW, a displacement constraint of out-of-plane is applied at the reference point.

2.4. Model verification

Based on the above Settings, SCSW4 specimens in reference [36] were selected for modeling to ensure correctness of parameters of the FE model. The size and loading mode of the FE model are same with test.

The failure mode and steel plate buckling position of the finite element analysis results are very similar to those of the test (Fig. 5). Both FE model and experimental test showed steel plate local buckling at the end of the specimen. This confirms the accuracy and reliability of the finite element simulation in predicting the failure mode of the DSCW. From the comparative analyses of the hysteresis curves and skeleton curves, it is evident that they all have very similar trends and the error in the curves is very small. However, during the specimen’s failure stage, the model predicts a slightly higher bearing capacity compared to the actual test value. This is caused by defects in the welding of steel plates and concrete placement during the production of samples.

(a)Test destructive mode

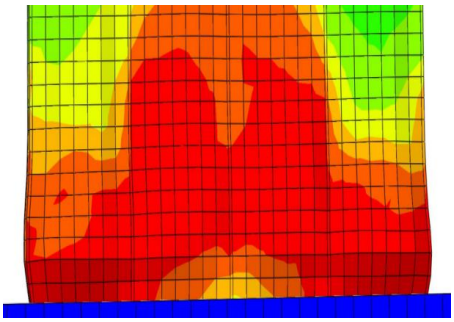

(b) Finite element destruction model

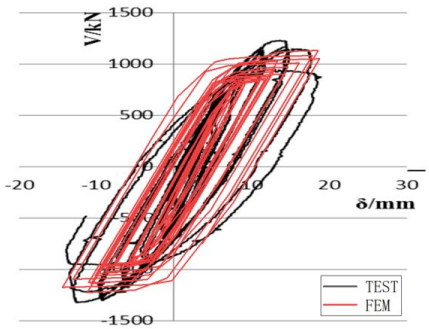

(c) Comparison of experimental and FE model hysteresis curves

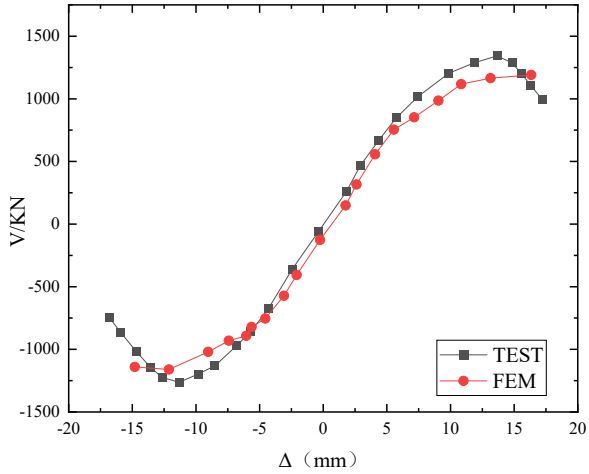

(d) Comparison of experimental and FE model skeleton curves

Fig. 5 Model validation

3. Parametric study

After verifying the test results using ABAQUS software, the study proceeded to investigate the seismic performance of DSCW with varying parameters. he effects of different parameters such as corrosion rate, plate thickness, concrete strength grade, and axial compression ratio, is examined in the parametric study. These variables significantly influence the mechanical properties of DSCW, highlighting the need to quantify their effects accurately. To realistically simulate the random corrosion scenarios encountered in practical engineering, corrosion models are generated using the random function in Python. These models simulate local corrosion rates on steel plates, ranging from 0% to 25%. This approach allows for a comprehensive evaluation of how varying corrosion levels affect the structural integrity and seismic behavior of DSCW.

3.1. Influence of the steel plate thickness

In this section, the influence of steel plate thickness on corroded DSCW bearing capacity is discussed (Table 1). DSCW specimens with steel plate thicknesses of 5 mm to 9 mm, and corrosion rates of 0% to 25%, are designed. The shear walls have a height-to-width ratio of 1.0, a concrete strength grade of C30, restraining tie bars with diameters of 10 mm, and steel plates made of Q235 material. FE-C1 to FE-C3 represent specimens with varying steel plate thicknesses, while FE-C1-0 to FE-C1-2-25 represent specimens with different corrosion rates.

Table 1
Design parameters of specimens

Test specimen	Steel plate thickness（mm）	Concrete strength grade	Axial compression ratio	Corrosion rates（%）
FE-C1-0	5	C30	0.2	0
FE-C1-10	5	C30	0.2	10
FE-C1-15	5	C30	0.2	15
FE-C1-25	5	C30	0.2	25
FE-C2-0	7	C30	0.2	0
FE-C2-10	7	C30	0.2	10
FE-C2-15	7	C30	0.2	15
FE-C2-25	7	C30	0.2	25
FE-C3-0	9	C30	0.2	0
FE-C3-10	9	C30	0.2	10
FE-C3-15	9	C30	0.2	15
FE-C3-25	9	C30	0.2	25

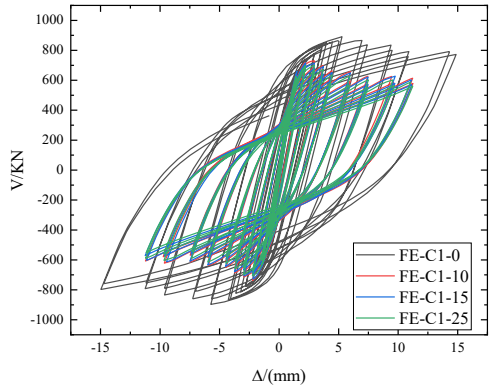

(a)FE-C1

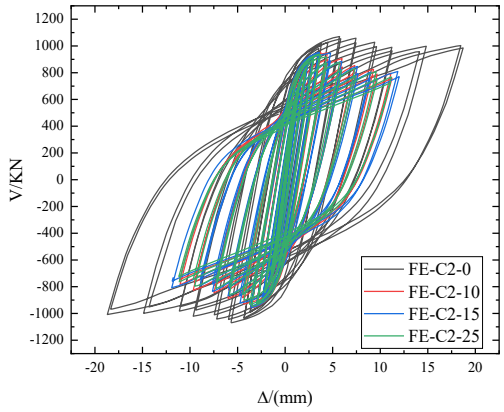

(b)FE-C2

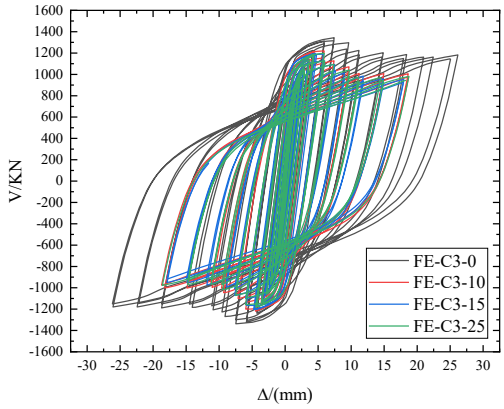

(c)FE-C3

Fig. 6 The hysteresis curves of different thicknesses of steel plate

Table 2
Peak load

Specimen number	Peak load
FE-C1-0	890.80
FE-C1-10	733.45
FE-C1-15	722.42
FE-C1-25	703.17
FE-C2-0	1177.03
FE-C2-10	1050.43
FE-C2-15	1046.11
FE-C2-25	1036.97
FE-C3-0	1343.01
FE-C3-10	1218.33
FE-C3-15	1200.75
FE-C3-25	1189.10

3.1.1. Hysteresis curve analysis

The hysteresis curve of FE-C3 is fuller than that of FE-C2 (Fig. 6), it shows that an increase in steel plate thickness may provide greater confinement to the concrete, thereby reducing concrete cracking. However, the hysteresis curves of specimens FE-C3-10, FE-C3-15, and FE-C3-25 gradually exhibit reduced fullness, indicating a weakening of energy dissipation capacity in corroded specimens. This trend highlights the significant detrimental effect of local corrosion on DSCW.

Among the specimens listed in Table 2, FE-C3-0 exhibits the highest peak load of 1343.01 kN. This value is 14.1% higher than that of FE-C2-0. With a constant corrosion rate, the peak load increases gradually with increasing steel plate thickness, indicating that a thicker steel plate enhances the shear wall's bearing capacity. Specifically, the peak load of FE-C3-0 is 10.2% higher than that of FE-C3-10. Conversely, with a constant steel plate thickness, the peak load decreases as the corrosion rate increases, show a reduced bearing capacity due to increased corrosion. Furthermore, the increase in peak load is more pronounced for specimens with 9 mm steel plate thickness compared to those with 7 mm at the same local corrosion rates. This observation underscores that thicker steel plates contribute to improved seismic performance and energy dissipation capacity, making them more resilient to corrosion.

3.1.2. Skeleton curve analysis

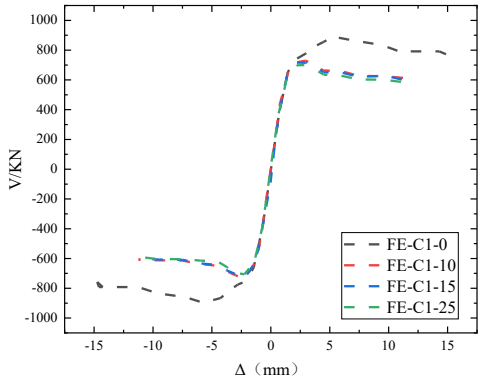

(a)FE-C1

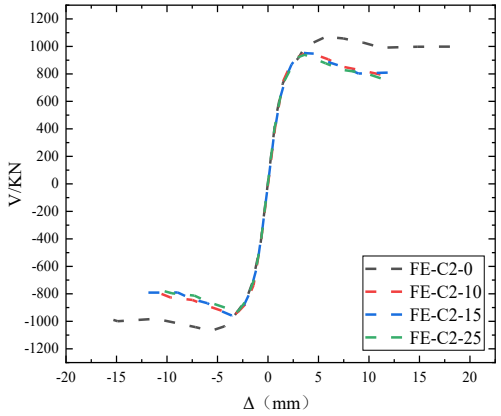

(b)FE-C2

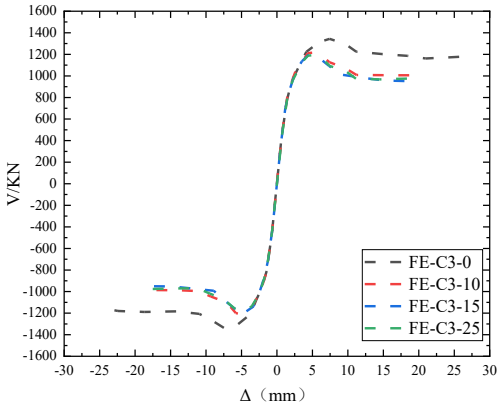

(c)FE-C3

Fig. 7 The skeleton curve of different thicknesses of steel plate

By processing the hysteresis curves, the skeleton curves are derived and shown in Fig. 7. Each specimen's skeleton curve exhibits three distinct stages. The following observations can be made from Fig. 7 (a-c): In the elastic stage, the curvature remains consistent, suggesting that corrosion has minimal effect on the initial stiffness of the DSCW. In the plastic stage, the curvature the curve diminishes significantly, and all specimens exhibited inflection points. The inflection points of specimens with corrosion rates of 10%–25% occurred significantly earlier than those of the uncorroded specimens. This is due to corrosion reducing the stiffness of the steel plate, causing it to yield prematurely. The inflection points of the FE-C3 series specimens occurred later than that of the FE-C2 and FE-C1 series specimens. This is primarily due to the increased thickness of the steel plate, which significantly enhances the lateral stiffness of the DSCW. During the failure stage, the curve shows a progressively steeper decline with increasing corrosion rates. The strength of the FE-C1-25 specimens decreased significantly, while the FE-C3-0 and FE-C2-0 specimens performed the best throughout the failure stage. The results show that increased steel plate corrosion diminishes the DSCW 's peak load, ductility, and deformation capacity. Increasing the thickness of steel plate can significantly improves the seismic performance of corroded DSCWs, but it reduces ductility. In practice, the thickness of steel plate can be appropriately increased to mitigate the negative impact of corrosion and enhance seismic performance of DSCW.

3.2. Influence of the concrete strength grade

In this section, the influence of concrete strength on corroded DSCW bearing capacity is discussed. DSCW specimens are designed using FE-C1 as the base model, with local corrosion rates of 0%, 10%, 15%, and 25%, and concrete strength grades of C30 to C50. The parameters for each model are shown in Table 3.

Table 3
Design parameters of specimens

Test specimen	Steel plate thickness (mm)	Concrete strength grade	Axial compression ratio	Corrosion rates (%)
FE-C1-0	5	C30	0.2	0
FE-C1-10	5	C30	0.2	10
FE-C1-15	5	C30	0.2	15
FE-C1-25	5	C30	0.2	25
FE-E1-0	5	C40	0.4	0
FE-E1-10	5	C40	0.4	10
FE-E1-15	5	C40	0.4	15
FE-E1-25	5	C40	0.4	25
FE-E2-0	5	C50	0.2	0
FE-C3-10	9	C30	0.2	10
FE-C3-15	9	C30	0.2	15
FE-C3-25	9	C30	0.2	25

Table 4
Peak load

Specimen number	Peak load
FE-C1-0	890.80
FE-C1-10	733.45
FE-C1-15	722.42
FE-C1-25	703.17
FE-E1-0	990.38
FE-E1-10	817.73
FE-E1-15	827.90
FE-E1-25	824.51
FE-E2-0	1005.5
FE-E2-10	880.37
FE-E2-15	871.23
FE-E2-25	858.40

3.2.1. Hysteresis curve analysis

An increase in the concrete strength grade from C30 (FE-C1-0) to C40 (FE-E1-0) resulted in a rise in the overall stiffness of the specimens, as well as a significant increase in the peak load, which increased by 11.18% (Fig. 8, Table 4). However, when the concrete strength was further elevated from C40 (FE-E1-0) to C50 (FE-E2-0), the peak load showed only a modest increase of 1.53%. With the increase of concrete strength, the effect on the peak load of DSCW decreases gradually. In the case of corroded DSCWs, when the corrosion rate increased from 0% to 10%, the peak horizontal bearing capacity of specimens with concrete strengths ranging from C30 to C50 decreased by 17.66%, 17.43%, and 12.44%, respectively. The reduction in peak load of corroded DSCW was effectively mitigated with the concrete strength grade added.

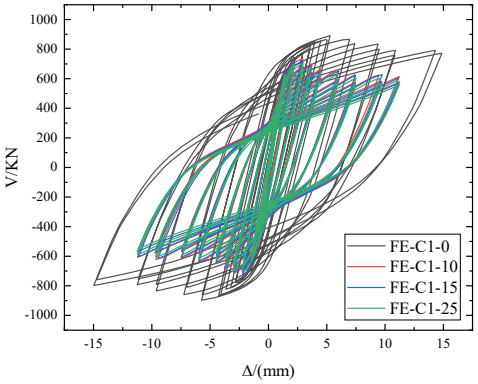

(a)FE-C1

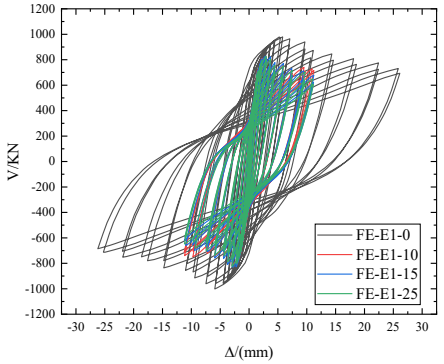

(b)FE-E1

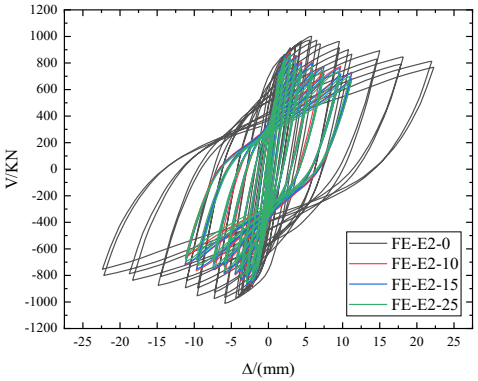

(c)FE-E2

Fig. 8 The hysteresis curves of different concrete strength grades

3.2.2. Skeleton curve analysis

The elastic and plastic stages of the skeleton curve are similar (Fig. 9). The peak load of the FE-E1 series specimens exceeds that of the FE-C1 series, but is lower than that of the FE-E2 series specimens. This suggests that, for the same corrosion rates, an increase in concrete strength grade gradually improves the peak load of the DSCW. Under non-corrosive conditions, the elastic and plastic stages of the skeleton curve exhibit similar characteristics, with a gradual decline observed in the failure stage. However, at corrosion rates of 10%, 15%, and 25%, the disparity in the skeleton curves increases as the concrete strength grade increases. This indicates that higher concrete strength, combined with increased corrosion rates, leads to greater variations in the shear wall's bearing capacity.

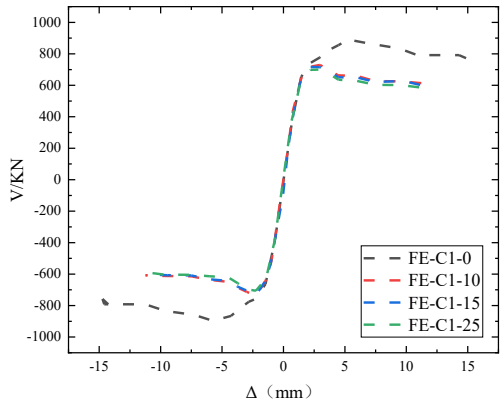

(a)FE-C1

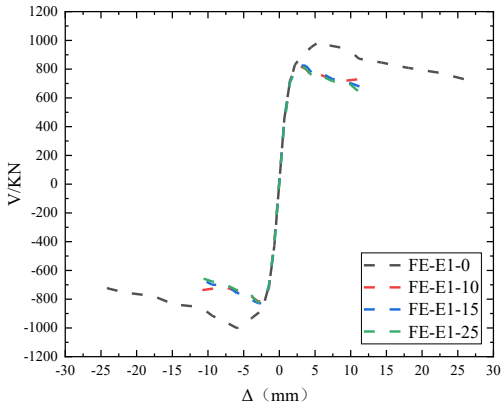

(b)FE-E1

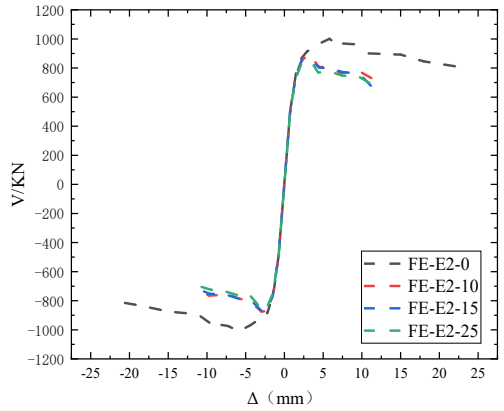

(c)FE-E2

Fig. 9 The skeleton curve of different concrete strength grades

3.3. Influence of the axial compression ratio

In this section, the axial compression ratio is the primary research parameter, while other parameters remain constant. DSCW specimens are designed with local corrosion rates of 0%, 10%, 15%, and 25%, and axial compression ratios from 0.2 to 0.6. The parameters for each model are provided in Table 5.

3.3.1. Hysteresis curve analysis

As shown in Fig. 10, In the case of no corrosion, the hysteresis loop pinching phenomenon more serious with the increase of axial compression ratio. This suggests that the energy dissipation capacity of DSCW decreases with the increase of axial compression ratio. Upon examining the hysteresis curve of FE-F1-0, an upward phase is observed after the initial decline. This phenomenon is caused by the buckling of the steel plate and the crushing of concrete in the DSCW. However, the binding bars continue to restrain the steel plate after buckling, preventing excessive deformation and extensive concrete crushing. Therefore, the bearing capacity has an upward trend when the shear wall continues to load.

Table 5
Design parameters of specimens

Test specimen	Steel plate thickness （mm）	Concrete strength grade	Axial compression ratio	Corrosion rates （%）
FE-C1-0	5	C30	0.2	0
FE-C1-10	5	C30	0.2	10
FE-C1-15	5	C30	0.2	15
FE-C1-25	5	C30	0.2	25
FE-F1-0	5	C30	0.4	0
FE-F1-10	5	C30	0.4	10
FE-F1-15	5	C30	0.4	15
FE-F1-25	5	C30	0.4	25
FE-F2-0	5	C30	0.6	0
FE-F2-10	5	C30	0.6	15
FE-F2-15	5	C30	0.6	15
FE-F2-25	5	C30	0.6	25

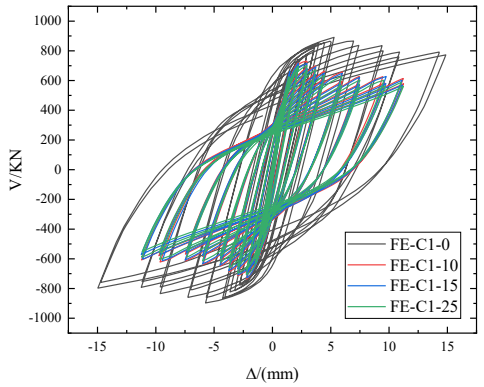

(a)FE-C1

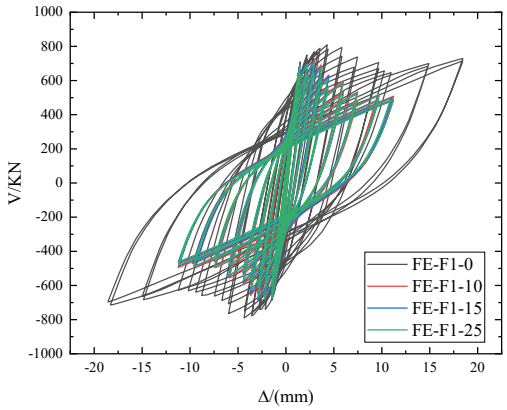

(b)FE-F1

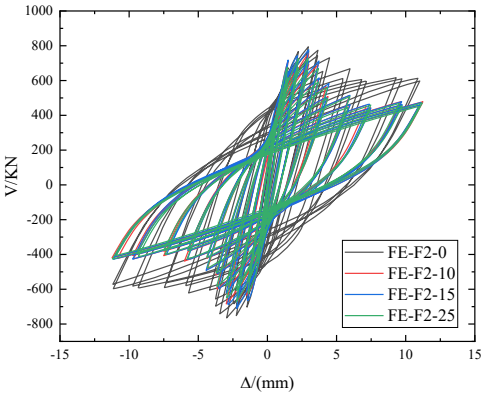

(c)FE-F2

Fig. 10 The hysteresis curves of different axial compression ratios

Table 6
Peak load

Specimen number	Peak load
FE-C1-0	890.80
FE-C1-10	733.45
FE-C1-15	722.42
FE-C1-25	703.17
FE-F1-0	799.91
FE-F1-10	698.94
FE-F1-15	693.97
FE-F1-25	689.18
FE-F2-0	779.59
FE-F2-10	719.64
FE-F2-15	743.38
FE-F2-25	700.07

At an axial compression ratio of 0.6, an increase in corrosion rates result in a marked reduction in the specimen's peak load, as indicated by the steeper descending section of the hysteresis curve. This trend indicates that higher axial compression ratios accelerate the decline in bearing capacity under seismic loading, potentially resulting in brittle failure. Consequently, in the practical engineering design of shear walls, it is advisable to regulate the axial compression ratio to mitigate substantial reductions in both bearing capacity and energy dissipation.

3.3.2. Skeleton curve analysis

The effect of the axial compression ratio on the seismic performance of the specimen is evident from the skeleton curve (Fig. 11). During cyclic loading, failure occurs in the corroded sections of the steel plate, resulting in buckling and reduced ductility of the DSCW. Comparing skeleton curves at different corrosion rates shows that corrosion significantly impacts the plastic phase. However, the trend in the failure phase shows minimal variation with increasing corrosion rates.

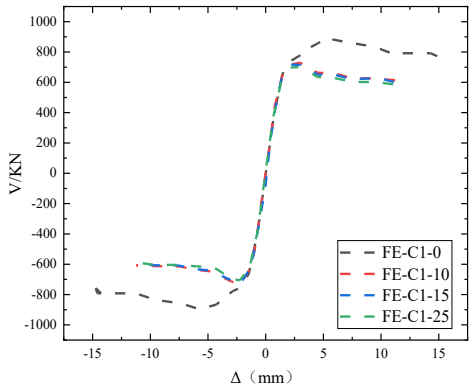

(a)FE-C1

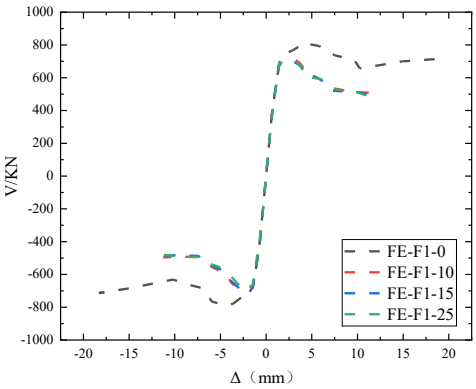

(b)FE-F1

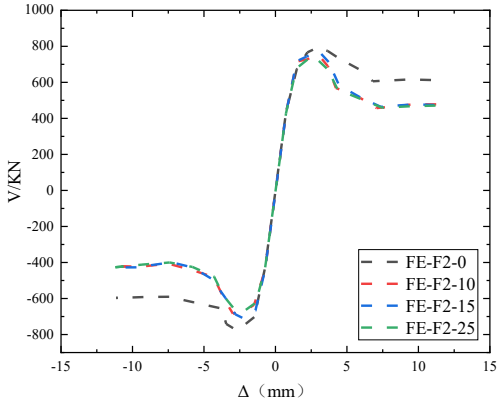

(c)FE-F2

Fig. 11 The skeleton curves different axial pressure ratios

4. Calculation of shear capacity of DSCW

Currently, the research on the shear capacity of DSCW has received widespread attention in both domestic and international academic circles. However, no existing specification specifically addresses the horizontal bearing capacity of corroded DSCW with binding bars. Therefore, a shear capacity formula specifically for DSCW with binding bars was proposed and assesses its effectiveness in predicting their shear capacity.

4.1. Calculation of shear capacity formula for DSCW

This paper studied the mechanical properties of DSCWs consisting of steel plates, concrete, and binding bars. These components work together to enhance the shear bearing capacity of the DSCW. While steel plates and concrete directly offer to the shear capacity, the binding bars provide indirect protection to the concrete by restricting steel plate buckling, a factor critical to maintaining shear capacity.

Finite element analysis shows that parameters significantly influence the seismic performance of these shear walls. To accurately quantify the shear bearing capacity, the formula from the specification [37] is modified to include the contribution of binding bars. This modification is based on least squares fitting of finite element simulation data using SPSS software, as detailed in Eq. (2) of this paper.

$$V \le \frac{1}{\gamma_{RE}}\left[\frac{0.12 f_t b_w h_w}{(\lambda-0.5)}+\frac{0.036 f_c b_w h_w}{(\lambda-0.5)}+\frac{0.2 f_y A_s h_w}{H}+0.16 f_{ys} A_{st}\right] R^2 = 0.95 \quad (2)$$

Where γ_{RE} is seismic adjustment factor for load capacity, f_t is design value of axial tensile strength of concrete, b_w is thickness of DSCW, h_w width of DSCW, λ is shear span ratio, f_c is design value of axial compressive strength of concrete, A_s is full cross-sectional area of steel plate in section, H is height of DSCW, f_{ys} is design value of tensile strength of binding bars, A_{st} is cross sectional area of binding bars.

The calculation of the above specimens was performed using Eq. (1), and the calculating results were compared with the FE values (Table 7).

The comparison reveals that the average ratio between finite element calculated values and the theoretical formula results is 0.930. The calculated value from the finite element method good agreement with the value obtained from the formula. Therefore, Eq. (2) for shear capacity is highly applicable, accurately estimating the shear capacity of the DSCW.

Table 7
Comparison of the finite element calculated values and calculated values of the formula

Specimen number	Finite element calculated value V_f/(kN)	Formula value V_c/(kN)	V_f/V_c
FE-C1-0	812.37	890.80	0.91
FE-F1-0	812.37	799.91	1.02
FE-C2-0	1021.35	1170.03	0.88
FE-E1-0	899.46	990.38	0.91

4.2. Calculation of shear capacity formula of DSCW after partial corrosion

An extension of Eq. (2) for the shear capacity of DSCW has been developed to account for corrosion. This extension involves fitting a formula to express the horizontal bearing capacity of corroded DSCW. To quantify the influence of corrosion on shear capacity, the average ratio of the shear capacity of each corroded model relative to the uncorroded model has been determined. Subsequently, an equation has been derived to describe how this average ratio varies with the corrosion rate (Eq. (3)).

$$\frac{N'}{N} = 1 - 2.02x^2 + 1.521x - 0.899\sqrt{x} \quad R^2=0.92 \tag{3}$$

Where N' is the corrosion of the DSCW combination of shear capacity, N is the shear capacity of the uncorroded DSCW combination. x is the corrosion rate.

Eq. (2) and (3) have been combined to derive Eq. (4), which describes shear capacity of the corroded DSCW. The specific parameters of 16 specimens were substituted into Eq. (4) to calculate the horizontal bearing capacity of the DSCW, shown in Table 8.

$$N' \le \left(1 - 2.02x^2 + 1.521x - 0.899\sqrt{x}\right) \times \frac{1}{\gamma_{RE}}\left[\frac{0.12 f_t b_w h_w}{(\lambda - 0.5)} + \frac{0.036 f_c b_w h_w}{(\lambda - 0.5)} + \frac{0.2 f_y A_s h_w}{H} + 0.16 f_{ys} A_{st}\right] \tag{4}$$

Table 8
Comparison the finite element calculated values and theoretical formula results

Specimen number	Finite element calculated value V_t/(kN)	Formula value V_c/(kN)	V_t/V_c
FE-C1-0	812.37	890.8	0.91
FE-C1-10	688.58	733.45	0.94
FE-C1-15	677.94	722.42	0.94
FE-C1-25	653.55	703.17	0.93
FE-C2-0	1021.35	1063.66	0.96
FE-C2-10	865.71	954.94	0.91
FE-C2-15	852.34	951.01	0.90
FE-C2-25	821.68	942.70	0.87
FE-E1-0	899.46	990.38	0.91
FE-E1-10	762.39	817.73	0.93
FE-E1-15	750.61	827.9	0.91
FE-E1-25	723.61	824.51	0.88
FE-F1-0	812.37	799.91	1.02
FE-F1-10	688.58	698.94	0.99
FE-F1-15	677.94	693.97	0.98
FE-F1-25	653.55	689.18	0.95

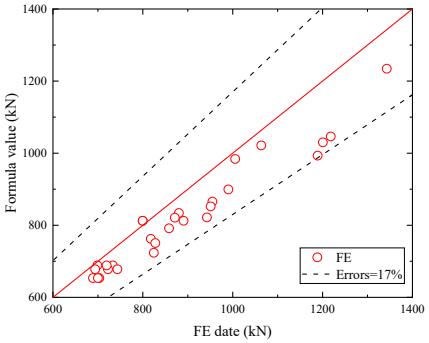

Fig. 12 Verification of calculation model

Table 8 compares the calculated values from the formula with those obtained through finite element analysis. The average ratio of the finite element calculation values to the theoretical formula results is 0.93. The finite element analysis data and formula calculation data are utilized to assess the accuracy of Eq. (4). The proposed formula clearly and accurately calculates the shear capacity of corroded DSCW, with a deviation of less than 17% (Fig. 12). In general, the theoretical formula can effectively calculate the shear capacity of DSCW. This formula provides a reliable basis for future engineering applications. It should be noted that the shear capacity formula for corroded DSCW proposed in this paper is specifically applicable to DSCW with local corrosion.

5. Residual seismic capacity

The seismic performance of buildings is reduced due to earthquakes, initial defects, and durability concerns. Assessing the residual seismic capacity of damaged structures is essential for preparing them for future earthquakes. Currently, the assessment of residual seismic capacity mainly involves assessing cracks and the post-earthquake behavior of structural components. This approach is subjective and requires extensive field investigations. Therefore, this study based on the energy dissipation capacity of DSCW to analyze their residual seismic capacity at each loading stage. The aim is to develop a seismic performance evaluation method for earthquake-damaged shear walls, using residual drift as the primary evaluation criterion.

5.1. Relative residual side shift and relative side shift correspondence

In the investigation of the seismic capacity of DSCW, residual drift is a crucial indicator for evaluating their resilience. A normalization approach is employed to conduct a quantitative analysis of residual drift. This involves dividing the drift (δ_{dr}) and residual drift (δ_{re}) at each loading stage by their respective values at the failure state. This normalization results in the relative drift ($\delta_{dr}/\delta_{dr,failure}$) and relative residual drift ($\delta_{re}/\delta_{re,failure}$). A model (Eq. 5) was developed to assess the characteristics of residual drift in shear wall specimens subjected to cyclic loading, as shown in Fig. 13(a).

$$\frac{\delta_{re}}{\delta_{re,failure}} = 0.84\left(\frac{\delta_{dr}}{\delta_{dr,failure}}\right)^2 + 0.16\frac{\delta_{dr}}{\delta_{dr,failure}} \tag{5}$$

The formula's coefficient of determination R^2 is 0.94, confirming the accuracy and applicability of predicting the residual drift of specimens at different drift states. To further validate the formula's applicability in predicting the relationship between relative residual drift and drift in DSCWs, test results from three specimens subjected to low cyclic loading, as reported in the literature [34], were selected for model validation (Fig. 13(b)). The computational analysis model shows a relatively small difference when compared to the relationship between relative residual drift and relative drift proposed in this paper, demonstrating that the model can be broadly applied to predict residual drift in various types of DSCW with ductile failure.

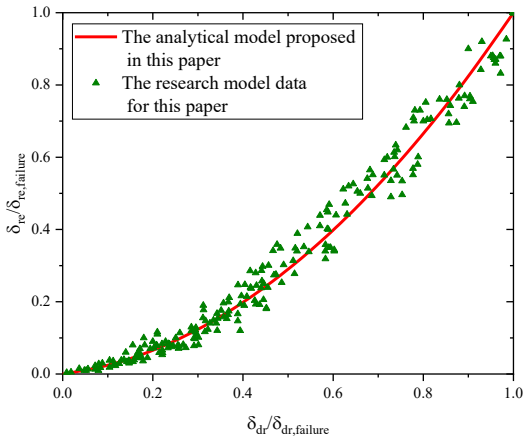

(a) Proposal of calculation model

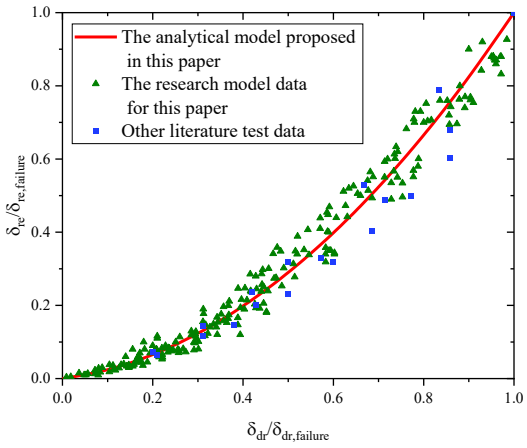

(b) Verification of calculation model

Fig. 13 The relationship of relative residual drift and relative drift for DSCW

5.2. Residual seismic capacity and reinforcement analysis

For assessment of the residual seismic capability of DSCW after earthquake damage, the residual seismic capacity discount factor R, put forward by JBDPA and Geng [38,39], is calculated based on Fig. 14, as shown in Eq. (6). The area under the skeleton curve from initial loading to the damaged state represents the total energy E_d. At any loading level, the area enclosed by the drift and residual drift on the skeleton curve represents the absorbed energy E_d. The residual absorbed energy E_r is then determined by subtracting the absorbed energy from the total energy.

$$R = \frac{E_r}{E_d + E_r} \tag{6}$$

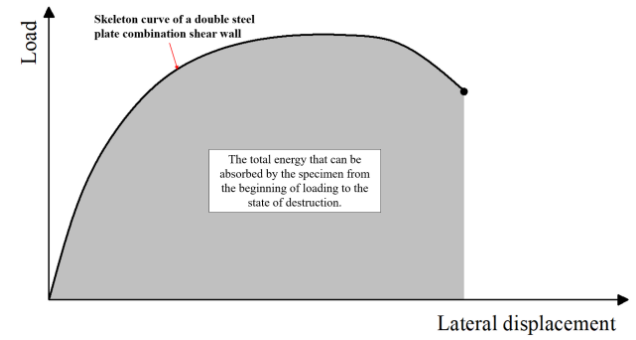

(a) Total absorbable energy

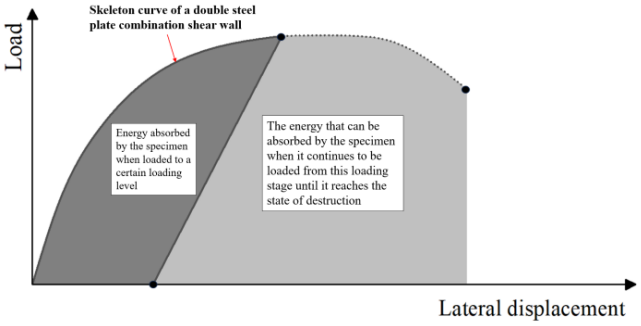

(b) Already absorbed energy

Fig. 14 Seismic capacity reduction factor for damaged DSCW

The residual seismic capacities of all shear wall specimens at different loading levels are combined (Fig. 15(a)). A fitting formula for the relative value of residual drift and residual seismic capacity is proposed, on the basis of the data degradation analysis method, as shown in Eq. (7). The coefficient of determination R^2 for this formula is 0.95, indicating that the results of DSCW calculated by this method's error is small.

To evaluate the accuracy and applicability of Eq. (7) in predicting the residual seismic capacity of earthquake-damaged shear walls using relative values of residual drift, shear wall specimens from the literature [37] are selected to validate the calculation model. The data points, shown in Fig. 15(b), are compared with the analytical model proposed in Eq. (7). This establishes the corresponding relationship between residual drift and residual seismic capacity in earthquake-damaged shear walls. Although the calculation model may slightly underestimate the average residual seismic capacity of earthquake-damaged shear walls approaching failure, it provides a more conservative and secure conclusion when assessing the safety of these shear walls.

$$R = 1 - 0.86\frac{\delta_{re}}{\delta_{re,failure}} \quad 0 \le \delta_{re} / \delta_{re,failure} \le 1 \tag{7}$$

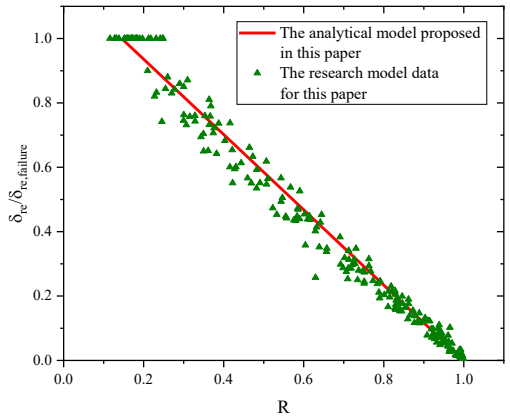

(a) Proposal of calculation model

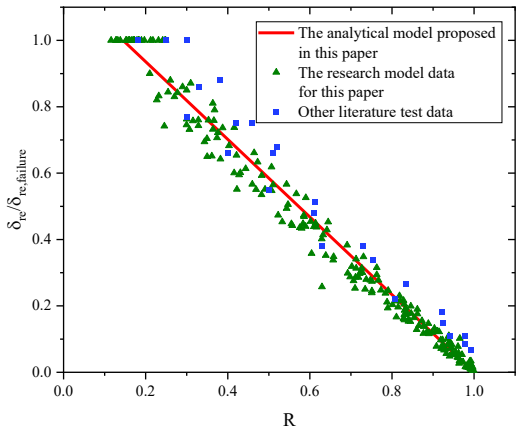

(b) Verification of calculation model

Fig. 15 Calculation model for the relationship of residual seismic capacity with relative residual drift for DSCW

Table 9
Evaluation index of damage evaluation for DSCW

Damage level	Residual seismic capacity	Relative Residual Side Shift
minimal	$R \ge 0.95$	$\delta_{re}/\delta_{re,failure} \le 0.06$
general	$0.75 \le R < 0.95$	$0.06 < \delta_{re}/\delta_{re,failure} \le 0.30$
medium	$0.50 \le R < 0.75$	$0.30 < \delta_{re}/\delta_{re,failure} \le 0.60$
severity	$R < 0.50$	$\delta_{re}/\delta_{re,failure} > 0.60$

To further investigate the post-earthquake reinforcement of earthquake-damaged DSCW, residual drift is used as the control criterion. A proposed relationship between shear wall failure grades and residual seismic capacity is presented in Table 9. The medium failure grade of the shear wall is designated as the benchmark for reinforcement assessment, with an average value of 0.45 being the recommended threshold for determining reinforcement needs. Therefore, when the relative value of residual drift exceeds 0.45, it indicates that the earthquake-damaged shear wall may no longer significantly benefit from continued reinforcement. Fig. 16 shows the residual drift of the shear wall at different corrosion rates in relation to the reinforcement limit based on residual drift.

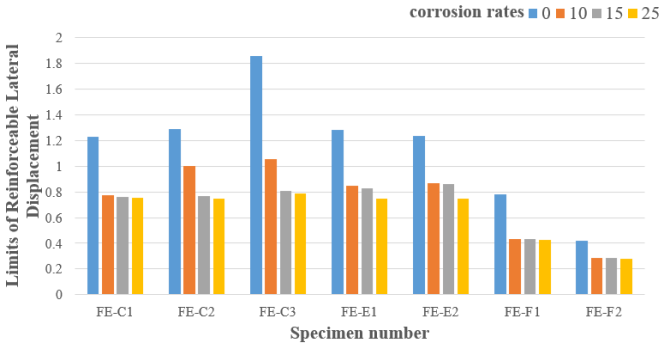

Fig. 16 The reinforcement limit based on residual drift

Compared to the uncorroded specimen, Corrosion of steel plate reduces its inhibition on internal concrete compared with non-corroded specimens. This results in less drift of the corroded specimen and less residual drift upon failure. The limit value of reinforced residual drift for the corroded specimen is also significantly reduced, with the reduction increasing as corrosion rates rise. At constant corrosion rates, both the thickness of the steel plate and the axial pressure ratio significantly affect the limit value of reinforced residual drift. Specifically, thicker steel plates gradually increase the limit value, although their impact diminishes as corrosion rates increase. Conversely, higher axial pressure ratios reduce the limit value. In practical applications, increasing the thickness of exterior steel plates in DSCW can enhance the limit value of reinforced drift. It is recommended to avoid components with high axial pressure ratios and to promptly assess reinforcement needs for corroded DSCWs in actual projects.

6. Conclusion

A detailed FE model of the corroded DSCW is developed in this paper. The model was validated through previous cyclic tests. On the basis of validation, different parameters were investigated. Based on the theoretical analysis, a formula for calculating corroded DSCW bearing capacity is proposed. The residual seismic capacity of the corroded DSCW is evaluated based on the energy dissipation, and the reinforced residual drift limit of the corroded DSCW after an earthquake is proposed. The main conclusions are drawn:

(1) The finite element analysis results demonstrate that corrosion significantly impacts the seismic performance of DSCW specimens, leading to consistent degradation in their bearing capacity. Corrosion diminishes energy dissipation, shear capacity, and ductility.

(2) The seismic performance of DSCW is primarily depends on variations in the constraint strength between the steel plate and concrete. The thickness of the steel plate is a crucial factor in determining the bearing capacity. As the thickness increases from 5 mm to 9 mm, shear capacity increases by 32.1% and 50.8%, respectively. Furthermore, the shear capacity of DSCW decreases linearly with increasing corrosion rates, regardless of other parameters.

(3) As corrosion levels rise, the bearing capacity of shear wall specimens decreases significantly, with a more pronounced reduction in displacement ductility compared to bearing capacity. Furthermore, increasing the axial compression ratio in corroded specimens leads to reductions in both bearing capacity and ductility. For DSCW subjected to significant corrosion, it is recommended that the axial pressure be controlled below 0.6 at the time of design.

(4) Considering both the effects of corrosion and the binging bars to bearing capacity, a shear capacity formula for DSCW incorporating both factors is proposed. Numerical simulation results validate the accuracy and applicability of this formula, with the maximum deviation remaining below 17%. Thus, the theoretical formulas can reliably predict the shear bearing capacity of DSCW.

(5) The residual seismic capacity at each loading stage for 28 specimens is evaluated using a modeling method based on the energy dissipation capacity of shear walls. The effectiveness of the proposed method is evaluated by calculating the relevant experiments. Additionally, a lateral displacement limit for DSCW after an earthquake is proposed, which can aid in the design of reinforcements for these structures.

References

[1] C.B. Wen, Y.L. Guo, H.J. Sun, et al. Experimental and numerical study on seismic performance of concrete-infilled double steel corrugated-plate walls[J]. Journal of Building Engineering, 2023, 68: 106171.

[2] Z.Q. Jiang, A.L. Zhang, L. Su, et al. Experimental study of axial compressive load capacity of internally stiffened double steel plate shear wall[J]. Journal of Constructional Steel Research, 2024, 216: 108566.

[3] Q. Luo, S. Zhao, W. Wang, et al. Research on interaction relationship and seismic performance efficiency of corrugated steel-plate composite shear wall[J]. Soil Dynamics and Earthquake Engineering, 2023, 172: 108046.

[4] Y. Qin, G.P. Shu, G.G. Zhou, et al. Compressive behavior of double skin composite wall with different plate thicknesses[J]. Journal of Constructional Steel Research, 2019, 157(JUN.):297-313.

[5] J. Li, F. Li, C. Liu, et al. Numerical and theoretical analysis of seismic behaviour of CFDSP composite shear walls. Journal of Building Engineering, 2020, 31: 101359.

[6] G.B. Lu, X.H. Zhou, Y.H. Wang, et al. Numerical investigation on circular concrete-filled double skin steel tube columns under torsion[C]. Structures. Elsevier, 2022, 37: 17-31.

[7] J.B. Yan, Z.X. Li, T. Wang. Seismic behaviour of double skin composite shear walls with overlapped headed studs[J]. Construction and Building Materials, 2018, 191: 590-607.

[8] L. Chen, S. Wang, Y. Lou, et al. Seismic behavior of double-skin composite wall with L-shaped and C-shaped connectors[J]. Journal of Constructional Steel Research, 2019, 160: 255-270.

[9] L. Chen, Q. Jin, J. Shi, et al. Seismic behavior of low shear-span ratio double-skin composite wall with L-shaped connectors[J]. Journal of Constructional Steel Research, 2022, 198: 107541.

[10] L. Zhu, D. Zhou, M. He, Experimental research on seismic behavior of composite concrete and steel plate shear walls with binding bars, [J]. Build. Struct. 2013, 6:93.

[11] W. Zhang, K. Wang, Y. Chen, et al. Experimental study on the seismic behaviour of composite shear walls with stiffened steel plates and infilled concrete[J]. Thin-Walled Structures, 2019, 144: 106279.

[12] L. Chen, C. Yin, C. Wang, et al. Experimental study on seismic behavior of double-skin composite wall with L-shaped connectors[J]. Journal of Constructional Steel Research,2020, 174:106312.

[13] S. Imperatore, Z. Rinaldi, C. Drago. Degradation relationships for the mechanical properties of corroded steel rebars[J]. Construction and Building Materials, 2017, 148: 219-230.

[14] X. Sun, H. Kong, H. Wang, et al. Evaluation of corrosion characteristics and corrosion effects on the mechanical properties of reinforcing steel bars based on three-dimensional scanning[J]. Corrosion Science, 2018, 142: 284-294.

[15] G. Qin, S. Xu, D. Yao, et al. Study on the degradation of mechanical properties of corroded steel plates based on surface topography[J]. Journal of Constructional Steel Research, 2016, 125: 205-217.

[16] L. Jin, X. Zhang, X. Liang, et al. Mechanical properties of corroded carbon steel based on random pit corrosion in marine environment[J]. Ocean Engineering, 2022, 260: 111759.

[17] R. Songbo, G. Song, K. Chao, et al. Fractal characteristic of corroded steel surface and application to the fracture analyses[J]. Construction and Building Materials, 2022, 340: 127759.

[18] Q. Yang, B. Zhao, B. Liu, et al. Influence of corrosion on loading capacity of circular concrete-filled steel tubular column[J]. Journal of Constructional Steel Research,2024,215108564-.

[19] Z. Zhao, T. Gao, X. Jian, et al. Eccentric compression capacity of circular CFST columns under random pitting corrosion[J]. Ocean Engineering, 2023, 288: 115975.

[20] S.S. Song, X. Liu, J. Chen, et al. Compressive behaviour of corroded thin-walled circular section steel stub columns[J]. Thin-Walled Structures, 2022, 180: 109794.

[21] Y. Wei, Z. Wu, X. Wang, et al. Mechanical behavior of locally corroded circular steel tube under compression[C]. Structures. Elsevier, 2021, 33: 776-791.

[22] F. Yuan, M. Chen, H. Huang, et al. Circular concrete filled steel tubular (CFST) columns under cyclic load and acid rain attack: Test simulation[J]. Thin-Walled Structures, 2018, 122: 90-101.

[23] S. Luo, M. Chen, H. Huang, et al. Eccentric compression test and ultimate load strength analysis of circular CFST long column with local corrosion[C]. Structures. Elsevier, 2023, 56: 104937.

[24] H. Huang, L. Guo, B. Qu, et al. Tests of circular concrete-filled steel tubular stub columns with artificial notches representing local corrosions[J]. Engineering Structures, 2021, 242: 112598.

[25] L. Zhong, L. Guo, C. Jia. Axial compression behavior of stub square concrete-filled steel tubes with regional defect[J]. Engineering Structures, 2023, 278: 115510.

[26] W. Xue, J. Chen, F. Xie, et al. Behavior of Corroded Thin-Walled Concrete-Filled Steel Tubular Stub Columns[J]. Buildings, 2022, 12(4): 481.

[27] F. Zhang, J. Xia, G. Li, et al. Degradation of axial ultimate load-bearing capacity of circular thin-walled concrete-filled steel tubular stub columns after corrosion[J]. Materials, 2020, 13(3): 795.

[28] C.L. Wang, Study on the monotonic and hysteretic constitutive relation of steel corrosion in general atmospheric environment, Xi'an University of Architecture and Technology, 2016.

[29] R. Wang, R. A. Shenoi. Experimental and numerical study on ultimate strength of steel tubular members with pitting corrosion damage[J]. Marine Structures, 2019, 64: 124-137.

[30] Y. Wang, X. Zhou, Z. Kong, et al. Effects of corrosion pits on the combined hardening behavior of low-carbon steel[J]. Construction and Building Materials, 2024, 447: 138058.

[31] S.T. Zhong, Concrete Filled Steel Tubular Structures, Tsinghua University Press, 2003.

[32] J. Lubliner, J. Oliver, S. Oller, et al. A plastic-damage model for concrete[J]. International Journal of solids and structures, 1989, 25(3): 299-326.

[33] J. Lee, G.L. Fenves. Plastic-damage model for cyclic loading of concrete structures[J]. Journal of engineering mechanics, 1998, 124(8): 892-900.

[34] A. Hillerborg, M. Modéer, P.E. Petersson. Analysis of crack formation and crack growth in concrete by means of fracture mechanics and finite elements[J]. Cement and concrete research, 1976, 6(6): 773-781.

[35] L.H. Han, G.H. Yao, Z. Tao. Performance of concrete-filled thin-walled steel tubes under pure torsion[J]. Thin-walled structures, 2007, 45(1): 24-36.

[36] Y.F. Luo, J. Li, X.N. Guo. Numerical analysis of hysteretic performance of double-steel-layer-concrete composite shear wall[J]. Journal of Hunan University, 2014, 41(6): 57-62.

[37] Harbin Institute of Technology. Steel Plate Shear Wall Technical Specification JGJ/T 380-2015[M]. China Architecture & Building Press,2016

[38] Guidelines for post-earthquake damage evaluation and rehabilitation[S]. Tokyo: Japan Building Disaster Prevention Association (JBDPA), 2001. (in Japanese)

[39] X.R. Geng. Evaluation procedures on post-earthquake residual drift and seismic capacity for RC columns. Harbin Institute of Technology, 2019